

Homology reveals significant anisotropy in the cosmic microwave background

Pratyush Pranav^{1,2, *} and Thomas Buchert¹

¹ Univ Lyon, ENS de Lyon, Univ Lyon1, CNRS, Centre de Recherche Astrophysique de Lyon UMR5574, F-69007, Lyon, France

² Department of Physics and Materials Science, University of Luxembourg, 162 A, Avenue de la Faiencerie, L-1511 Luxembourg City, Luxembourg

August 22, 2023

ABSTRACT

We test the tenet of statistical isotropy of the standard cosmological model via a homology analysis of the cosmic microwave background temperature maps. Examining small sectors of the normalized maps, we find that the results exhibit a dependence on whether we compute the mean and variance locally from the masked patch, or from the full masked sky. Assigning local mean and variance for normalization, we find the maximum discrepancy between the data and model in the galactic northern hemisphere at more than 3.5 s.d. for the PR4 dataset at degree-scale. For the PR3 dataset, the C-R and SMICA maps exhibit higher significance than the PR4 dataset at ~ 4 and 4.1 s.d. respectively, however the NILC and SEVEM maps exhibit lower significance at ~ 3.4 s.d. The southern hemisphere exhibits high degree of consistency between the data and the model for both the PR4 and PR3 datasets. Assigning the mean and variance of the full masked sky decreases the significance for the northern hemisphere, the tails in particular. However the tails in the southern hemisphere are strongly discrepant at more than 4 standard deviations at approximately 5 degrees. The p -values obtained from the χ^2 -statistic exhibit commensurate significance in both the experiments. Examining the quadrants of the sphere, we find the first quadrant to be the major source of the discrepancy. Prima-facie, the results indicate a breakdown of statistical isotropy in the CMB maps, however more work is needed to ascertain the source of the anomaly. Regardless, these map characteristics may have serious consequences for downstream computations such as parameter estimation, and the related Hubble tension.

Key words. Cosmology – Cosmic Microwave Background (CMB) radiation – primordial non-Gaussianity – topology – relative homology – topological data analysis

1. Introduction

The standard Lambda Cold Dark Matter (LCDM) paradigm of cosmology encapsulates and arises from the cosmological principle (CP), which posits that, on large enough scales, the Universe is isotropic and homogeneous (Peebles 1980, 1993; Durrer 2015). Though supported by strong mathematical, philosophical and historical foundations, the veracity of the fundamental tenets of CP has not yet been comprehensively and conclusively established, motivating theoretical and observational tests (Secrest et al. 2021; Oayda & Lewis 2023; Dam et al. 2023). The recent focus of cosmology towards data gathering and analysis presents us with an unprecedented opportunity to test the postulates of the cosmological principle, and the ensuing standard model of cosmology. The data gathered are from both the early and late epochs in the evolutionary timeline of the Universe, and have thrown up a number of surprises. Among others, this includes the famous discrepancy in the inference of the Hubble parameter between early- and late-Universe data (Di Valentino et al. 2021; Perivolaropoulos & Skara 2022; Aluri et al. 2023).

The Cosmic Microwave Background (CMB) radiation is one of the more important probes of the properties of the early Universe. Emitted at the epoch of recombination, when the Universe was merely 380,000 years old, the fluctuation characteristics of the CMB trace the fluctuation characteristics of the matter distribution in the early Universe (Durrer 2015; Jones 2017), and offer the largest and the oldest canvas on which to test the postulates

of CP. Therefore, studying the CMB fluctuations is essential towards understanding the properties of the stochastic matter field in the early Universe. The two components of the CMB radiation – temperature and polarization – present independent probes in to the properties of the primordial fluctuations (Durrer 1999; Seljak & Zaldarriaga 1997).

The general consensus is that the stochastic fluctuation field of the CMB is an instance of an isotropic and homogeneous Gaussian random field (Harrison 1970; Guth & Tye 1980; Starobinsky 1982; Guth & Pi 1982; Komatsu 2010); see also Buchert et al. (2017) and references therein for more recent investigations of Gaussianity. However, CMB data has thrown up a number of surprises in terms of anomalous features since the launch of the Cosmic Background Explorer (COBE) satellite (Fixsen et al. 1994). Due to its low resolution of approximately 7 degrees, the COBE satellite first discovered the truly large-scale anomalous lack of correlation in the CMB at 60 degrees and more. Subsequently, the Wilkinson Microwave Anisotropy Probe (WMAP) (Bennett et al. 2013) satellite with a higher resolution, discovered a number of other anomalies at smaller scales, that have persisted in the CMB measurements by the latest Planck satellite (Planck Collaboration et al. 2014a, 2016, 2020c). These anomalies which have been detected in both the real and the harmonic space, seem to be at odds with the postulates of the standard cosmological model, and perhaps with the more fundamental CP itself.

Representative examples of anomalies in the harmonic space consist of the *hemispherical power asymmetry* (HPA) (Eriksen

* Email:pratyuze@gmail.com

et al. 2004a; Hansen et al. 2009; Paci et al. 2010; Planck Collaboration et al. 2014b) or the *cosmic hemispherical asymmetry* (CHA) (Mukherjee & Souradeep 2016), the alignment of low multipoles (Schwarz et al. 2016), as well as the parity anomaly (Land & Magueijo 2005; Finelli et al. 2012; Planck Collaboration et al. 2014b). In particular, the power spectrum has been studied at large scales, for $\ell = 2, 40$ (Eriksen et al. 2004a; Mukherjee & Souradeep 2016), which has later been extended to smaller scales $\ell \sim 600$ (Hansen et al. 2009; Paci et al. 2010; Planck Collaboration et al. 2014b), and the analysis presents the evidence for HPA/CHA at all scales. Important to note is that the assumption of cosmological isotropy is challenged in other datasets as well (Bouchet et al. 2001; Colin et al. 2019; Secrest et al. 2021, 2022; Oayda & Lewis 2023; Dam et al. 2023). In particular, the analysis of galaxy survey datasets also points to a hemispherical asymmetry, as the northern and the southern galactic hemispheres appear to have different topo-geometrical characteristics (Kerscher et al. 1997, 1998, 2001; Appleby et al. 2022).

The anomalies in the real space have consisted of the discovery of the *cold-spot* (Cruz et al. 2005), as well as the unusual behavior of descriptors emerging from topo-geometrical considerations which involve the integral-geometric Minkowski functionals (MFs), particularly the genus statistic as a member of the MFs, first performed on WMAP data (Park 2004; Eriksen et al. 2004b), and later extended to Planck data (Planck Collaboration et al. 2014b, 2016, 2020c; Pranav et al. 2019a; Pranav 2021a, 2022). While Park (2004) perform their analysis on small sub-degree scales, Eriksen et al. (2004b) perform a multi-scale analysis spanning a range of sub- and super-degree scales. In both the cases, there are reported asymmetry between the CMB hemispheres, where the small scale analysis in Park (2004) reports anomalous behavior to the tune of 2σ , while (Eriksen et al. 2004b) report a more than 3σ deviation in the genus statistic at scales of approximately 5 degrees for negative thresholds. In this context, it is important to note that the purely geometric entities of the MFs, such as the area, contour length and skeleton length have consistently shown a congruence between the data and the model (Planck Collaboration et al. 2016; Buchert et al. 2017), while the topological entities such as the genus and the Euler characteristic have shown deviations between the data and the model (Eriksen et al. 2004b; Park 2004; Pranav et al. 2019a; Pranav 2021a, 2022).

Extending these studies, in this paper, we examine specific sectors of the CMB temperature maps with a view to test the tenet of statistical isotropy, via tools that find basis in purely topological notions arising from homology (Munkres 1984; Edelsbrunner & Harer 2010; Pranav 2015; Pranav et al. 2017) and its hierarchical extension persistent homology (Edelsbrunner et al. 2002; Edelsbrunner & Harer 2010; Pranav 2015; Pranav et al. 2017; Pranav 2021), which form the basis of the recently emerging field of topological data analysis (TDA) (Carlsson 2009; Porter et al. 2023). Using these methodologies, which form the basis for the developed computational pipeline tailored to examining the CMB datasets (Pranav 2022), the central contribution of this paper is the uncovering of a number of anomalous signatures, which point to different behavior of galactic hemispheres, that have evidence in the documented literature, but have been overlooked, and not given due attention in the past.

The advent of TDA holds important place in view of the recent surge in data acquisition in cosmology and astronomy, which demand increasingly more sophisticated tools to condense meaningful information from these large and growing datasets. In view of these observations, the tools and methodologies pre-

sented here particularly stand out as promising candidates to reveal novel features in the big cosmological datasets, including the completed, on going, and upcoming CMB observations as evidenced in this paper, as well as galaxy surveys. Even though a recent development, TDA has already witnessed a strong presence in a wide range of astrophysical research from studying the large scale structure of the Universe (van de Weygaert et al. 2011; Sousbie 2011; Shivashankar et al. 2016; Xu et al. 2018; Cisewski-Kehe et al. 2018; Feldbrugge et al. 2019; Biagetti et al. 2021; Kono et al. 2020; Wilding et al. 2021; Cisewski-Kehe et al. 2022; Ouellette et al. 2023), and the study of stochastic properties of astrophysical and cosmological fields in general (Park et al. 2013; Adler et al. 2017; Makarenko et al. 2018; Pranav et al. 2019b; Heydenreich et al. 2021; Pranav 2021b), including the CMB fluctuation field (Adler et al. 2017; Pranav et al. 2019a; Pranav 2021a, 2022).

Section 2 presents the data and methods, while Section 3 presents the main results. We discuss the results and conclude in Section 4.

2. Data and Methods

In this section, we briefly describe the data and methods employed at arriving the results. The computational pipeline, specifically tailored to the CMB data, but useful for the analysis of other scalar functions on \mathbb{S}^2 , is a recent development, and a detailed account may be found in Pranav et al. (2019a) and Pranav (2022).

2.1. Data

The data that we investigate are the temperature maps from the latest two data releases by the Planck team – Planck Data Release 3 (DR3), and the fourth and final, Planck Data Release 4 (DR4). These data releases represent a natural evolution of the Planck data processing pipeline, where the final data release incorporates the best strategies for both the LFI and HFI instruments, commensurate with an overall reduction in noise and systematics (Planck Collaboration et al. 2020b). The PR3 and the PR4 data sets are accompanied by 600 and 300 simulations respectively, that originate from the standard Λ CDM paradigm, which posits the CMB field to be an instance of an isotropic and homogeneous Gaussian random field. The PR3 dataset consists of observational maps obtained via four different component separation methods, namely C-R, NILC, SEVEM and SMICA, (c.f. Planck Collaboration et al. (2020a)). We analyze all the four maps in only one experiment, to assess the overall trend and congruence of results between the different component separation methods. This choice is dictated by significant computational overhead, especially for higher resolutions.

2.2. Methods

The methods employed in this paper emerge from algebraic and computational topology, at the level of homology (Munkres 1984; Edelsbrunner & Harer 2010) and persistent homology (Edelsbrunner et al. 2002; Edelsbrunner & Harer 2010). On \mathbb{S}^2 , only the 0- and 1D homology groups are of interest, which are associated with isolated components and holes of the excursion sets of \mathbb{S}^2 . These methodologies are complementary in nature to the integral-geometric Minkowski functionals (Eriksen et al. 2004b; Schmalzing & Buchert 1997; Schmalzing & Gorski 1998; Matsubara 2010; Ducout et al. 2013; Buchert et al.

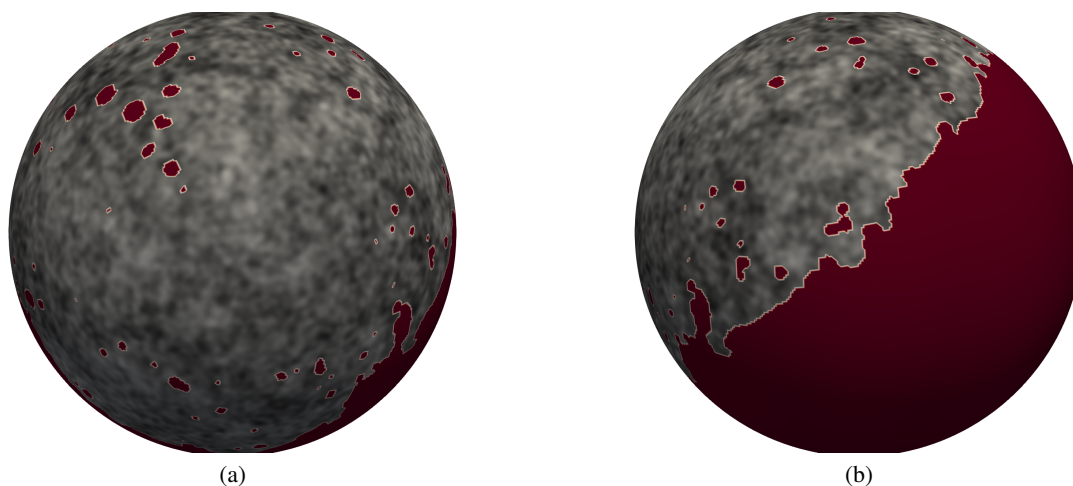


Fig. 1: A visualization of the CMB temperature fluctuation field in the northern hemisphere in two different views. The masked area covers the whole southern hemisphere, and the relevant parts of the northern hemisphere, dictated by the PR3 temperature common mask. The visualization is based on the PR3 observed map, cleaned using the SMICA component separation pipeline, degraded at $N = 128$ and smoothed with a Gaussian of $FWHM = 80'$.

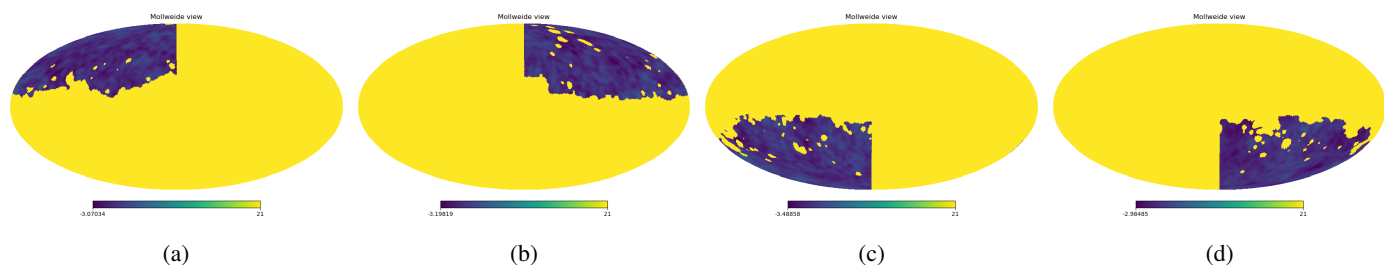


Fig. 2: An illustration of the analyzed map surface in the different quadrants of the sphere. The first, second, third and fourth quadrants are presented from left to right, and this convention is followed for quoting the results.

2017; Appleby et al. 2018; Chingangbam et al. 2017; Telschow et al. 2019), and together they represent a comprehensive topological characterization of fields.

As the CMB data is unreliable in certain regions of the sky, we mask these regions. We present our results in terms of the homology of the excursion sets relative to the mask, denoting the number of components relative to the mask for a given normalized threshold ν as $b_0(\nu)$. Similar definition is adopted for the number of loops, $b_1(\nu)$ (Pranav et al. 2019a; Pranav 2022).

In continuation of the experiments detailed in Pranav et al. (2019a), Pranav (2021a), and Pranav (2022), in this paper we perform our investigations on the hemispheres and quads of the CMB sky, where these regions are defined with respect to the galactic coordinates. When analyzing the northern hemisphere, the whole southern hemisphere and the relevant parts of northern hemisphere are masked, and vice-versa. Similar masking procedure is adopted when examining the quads. Figure 1 presents a visualization of the temperature fluctuation field in the northern hemisphere, smoothed with a Gaussian beam profile of $FWHM = 80'$. Figure 2 presents a visualization of the quads of the CMB sky in Mollweide projection view.

We perform a multi-scale analysis by smoothing the original maps given at $FWHM = 5'$ and $N = 2048$, to a range of scales defined by Gaussian beam profile of $FWHM = 10', 20', 40', 80', 160', 320'$ and $640'$. In order to facilitate faster computations, the maps are also degraded to $N =$

1024, 512, 256, 128, 64, 32 and 16 in the HealPix format, prior to the smoothing operation. The mask is subjected to an identical degrading and smoothing procedure. This results in a non binary mask, which is re-binarized by setting all pixels above and equal to 0.9 to 1, and all pixels with smaller values to 0. The mask is applied to the simulations and observations, and they are transformed to zero-mean and unit-variance fields by subtracting the mean and re-scaling by the standard deviation. Denoting $\delta T(\theta, \phi)$ as the fluctuation field at (θ, ϕ) on \mathbb{S}^2 , $\mu_{\delta T}$ as its mean, and $\sigma_{\delta T}$ as the standard deviation, computed over the relevant pixels, we examine the properties of the normalized field:

$$\nu(\theta, \phi) = \frac{\delta T(\theta, \phi) - \mu_{\delta T}}{\sigma_{\delta T}}. \quad (1)$$

In all the experiments we restrict ourselves to $\nu \in [0 : 3]$ while examining b_0 , and $\nu \in [-3 : 0]$ while examining b_1 , commensurate with the fact that components are the dominant topological entities at positive thresholds, while loops are dominant for the negative thresholds.

After the pre-processing steps, performed with the aid of HealPix software (Górski et al. 2005), the data is subject to the topology computation pipeline, which briefly involves tessellating the points on the sphere, computing the upper-star filtration of this tessellation, constructing the boundary matrix of the filtration, and reducing the boundary matrix to obtain the 0- and

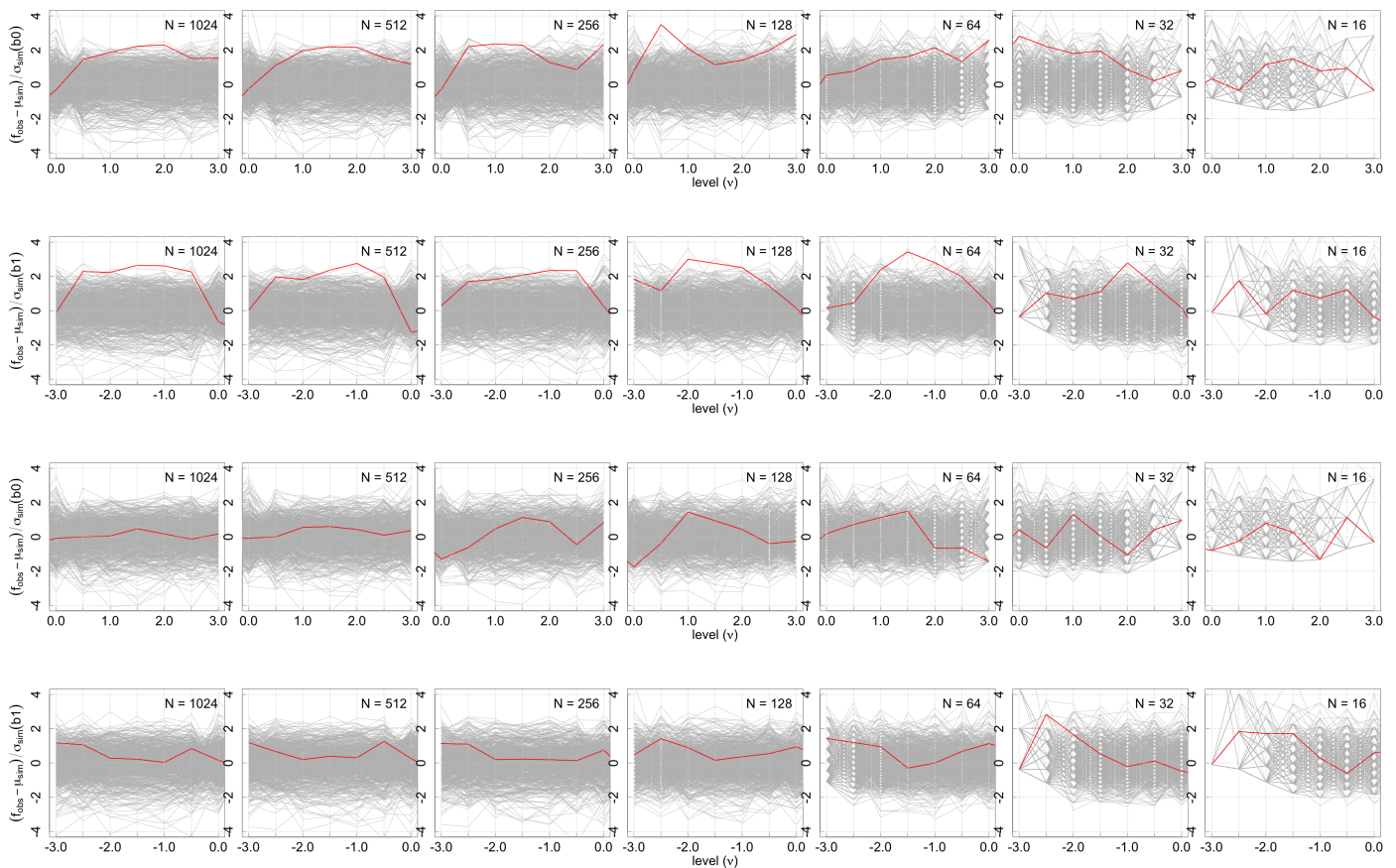


Fig. 3: Graphs of b_0 and b_1 for the temperature maps for the NPIPE dataset for the northern (top two rows) and the southern hemisphere (bottom two rows). The mean and variance are computed for each hemisphere locally from the unmasked pixels in that hemisphere. The graphs present the normalized differences, and each panel presents the graphs for a range of degradation and smoothing scales. The mask used is the PR3 temperature common mask.

1-dimensional persistence diagrams. The Betti numbers, relative to the mask are condensed from the persistence diagrams.

3. Results: Topological characteristics of subsets of \mathbb{S}^2

In this section, we present the results of the analysis of various sectors of the CMB sky, with a view to test statistical isotropy. We begin by presenting the results of examining the hemispheres, followed by an examination of the quads.

3.1. Hemispheres

For the hemispherical analysis, we present the results for two different experiments, which differ in the regions adopted for computing the mean and variance for normalizing the maps (c.f. (1)). In the first experiment, we compute the mean and variance for each hemisphere locally from the unmasked pixels. For the second experiment, we compute the mean and variance from the unmasked pixels from the full sky. In all the experiments, we present our results in terms of the graphs of the Betti numbers relative to the mask. The graphs are normalized at each threshold to reflect the significance of deviation. At each threshold, we compute the mean $\mu_{b_{i, sim}}$, and the standard deviation $\sigma_{b_{i, sim}}$ of the Betti numbers for $i = 0, 1$, corresponding to the components and the holes. Then, the significance of difference between the observation and simulations is given by

$$v_{b_i} = \frac{b_{i, obs} - \mu_{b_{i, sim}}}{\sigma_{b_{i, sim}}}, \quad (2)$$

which is the quantity depicted in the graphs.

3.1.1. Local normalization

For these experiments, the temperature at each pixel is mean-subtracted, and re-scaled by the standard deviation, where these quantities are computed locally from the unmasked pixels in each hemisphere. The topological quantities are computed as a function of the normalized temperature threshold, v , at steps of 0.5. Figure 3 presents the graphs for the significance of difference between the simulations and the observations, for the number of components, b_0 , and the number of loops, b_1 for the PR4 dataset. The red curve represents the observed sky, while the gray curves represent the individual simulations treated as observation. The top two rows present the graphs for b_0 and b_1 for the northern hemisphere, while the bottom two rows present the same for the southern hemisphere. Similar results for the PR3 dataset are presented in Figure A.3 in the appendix. For this case, we analyze all the four observational maps obtained from the different component separation pipeline.

We notice a few important things in the graphs. First, that both the PR4 and PR3 datasets present largely identical results.

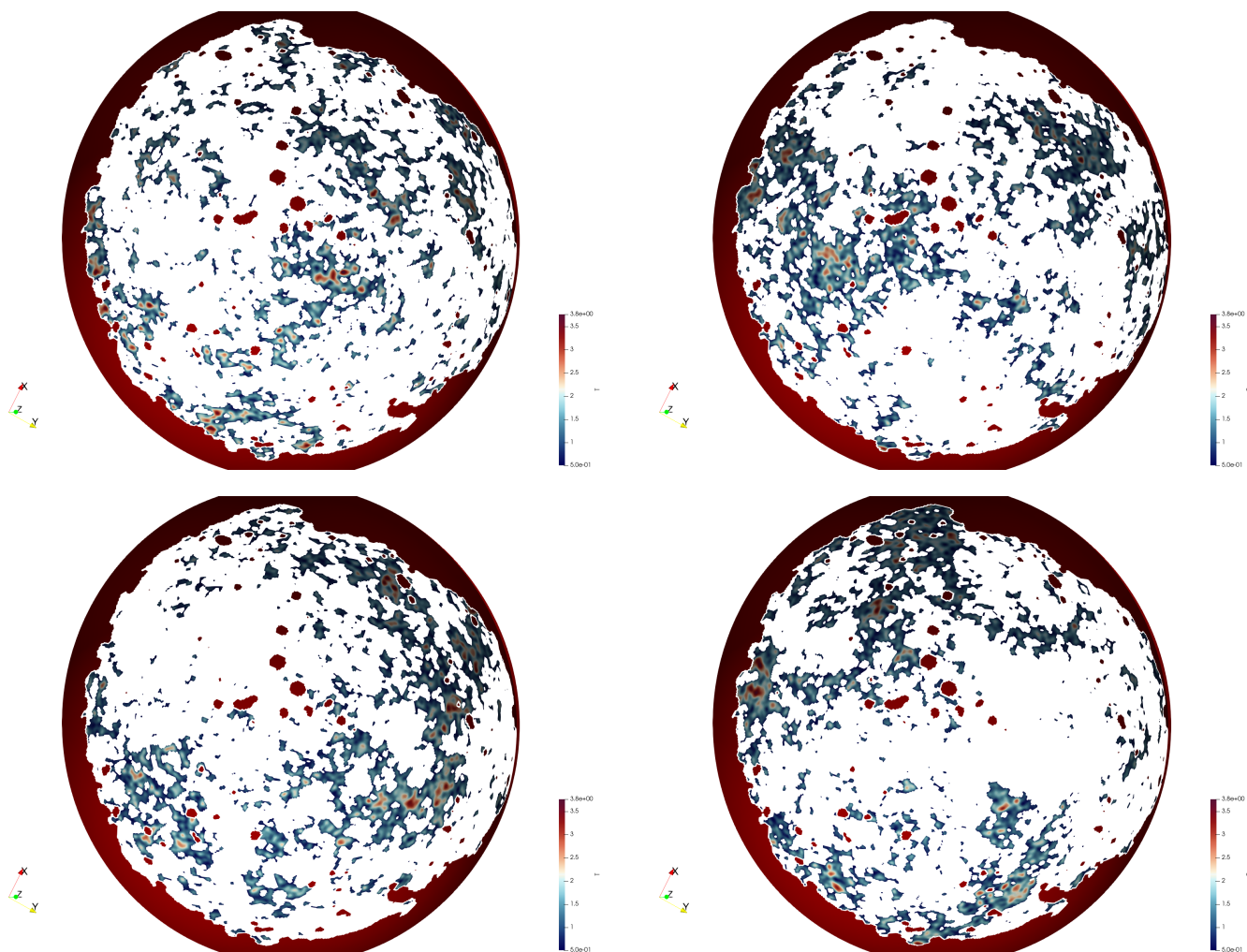


Fig. 4: A visualization of the structure of the superlevel set of the temperature field at the threshold $\nu = 0.5$ for the northern hemisphere. This is the threshold at which we detect a statistically significant deviation between the observation and simulations in the number of isolated components. Clock-wise from the top-left panel, we present the visualization of the observed CMB map from the FFP10 pipeline smoothed with a Gaussian beam profile of $FWHM = 80'$. The rest of the panels present the visualization for the randomly selected simulation sample numbering 42, and its two higher multiples 84 and 126. Visually, it is evident that the observational maps have more fragmented structure compared to the simulated maps.

Second, that the significance of deviation in the northern hemisphere is in general flared compared to the southern hemisphere. While the southern hemisphere significance is within the 2σ band in general, the northern hemisphere shows significance of 2σ or more for most of the scales. The third important thing that we notice is the very significant deviation in the number of components between the observations and simulations at the threshold $\nu = 0.5$, at $FWHM = 80'$, $N = 128$, which is at degree scale. The significance of difference for the PR4 datasets stands at approximately 3.5σ . For the PR3 dataset, two of the maps, namely C-R and SMICA, exhibit higher significance at approximately 4σ and 4.1σ respectively, while the two other maps, namely NILC and SEVEM, exhibit a 3.4σ deviation. Figure A.2 in the appendix presents the distribution of Betti numbers at this threshold, which maybe approximated as a Gaussian, which justifies ascribing a σ -significance to the differences. Figure 4 presents the visualization of the structure of the temperature field at $\nu = 0.5$ for the northern hemisphere. Clock-wise from top-left, we present the field for the observed CMB map, as well as three randomly selected simulated samples. It is evident that the observed maps

exhibit more fragmented characteristics than any of the visualized simulations, which engender the significant deviation in the number of components between the observation and the model.

For the loops, The highest deviation recorded is at $N = 64$, $FWHM = 160'$ for the northern hemisphere. The PR4 dataset exhibits a 3.4σ deviation, while the PR3 dataset shows a 3.2σ deviation at this scale. At $N = 128$, $FWHM = 80'$, the PR4 dataset exhibits a maximum of 3σ deviation, while the PR3 dataset exhibits a 2.6σ deviation.

3.1.2. Global normalization

Figure 5 presents the graphs similar to Figure 3 for the PR4 dataset, where the maps are normalized by the mean and variance computed from unmasked pixels from the full sky. Similar results for the PR3 dataset are presented in Figure A.4. As in the case of local normalization, we notice an agreement in the feature of the graphs between both the datasets. However, we also note important differences between observations and simulations. For the northern hemisphere, the significance of differ-

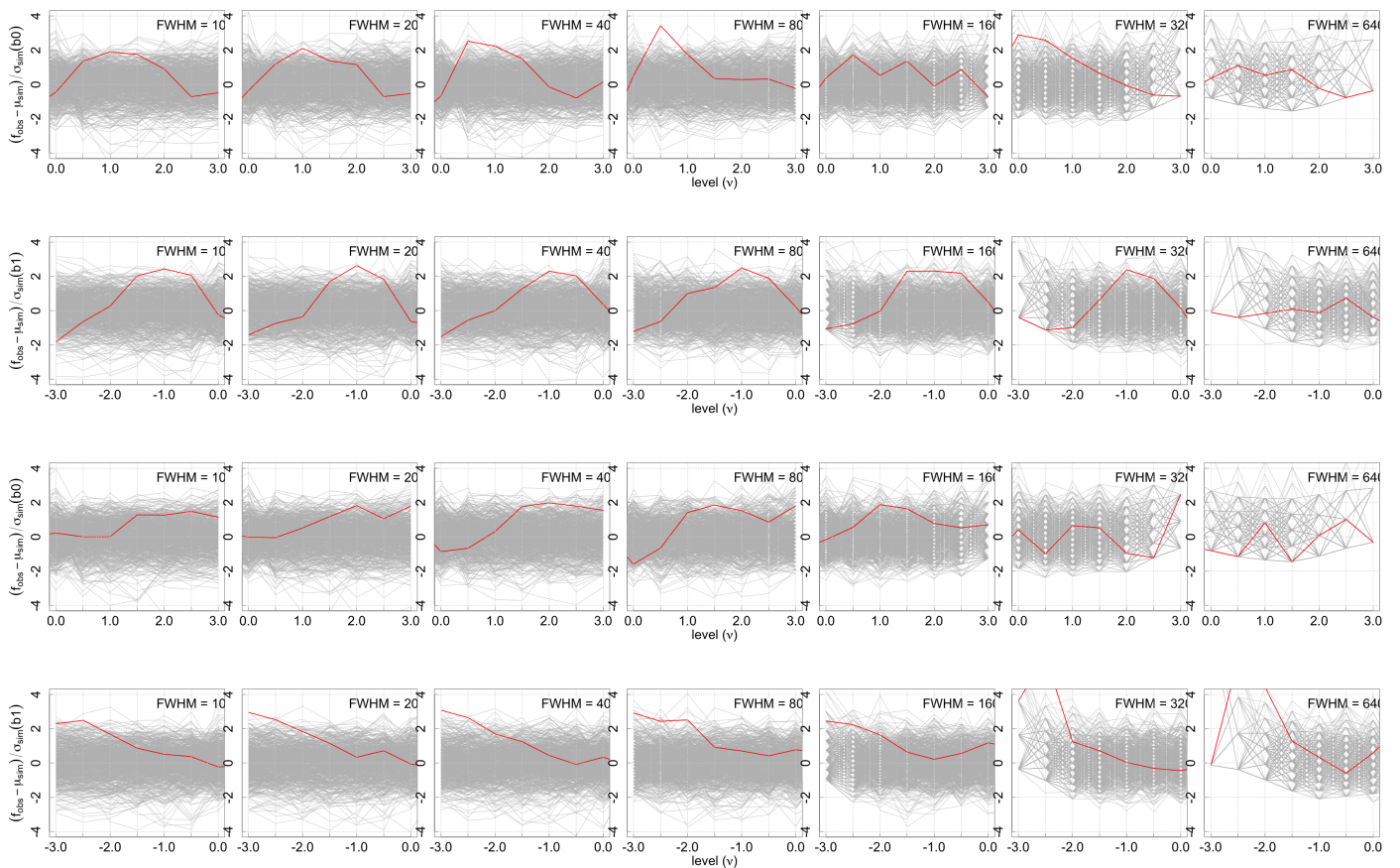


Fig. 5: Same as Figure 3, however in this case, the mean and variance are computed from the full sky from the unmasked pixels.

ence is slightly suppressed in general, and there is an evident change in the behavior of the tail, which is more in sync with the model. However, in this experiment, there are significant differences between the observation and the model in the southern hemisphere. While the number of components, b_0 , is generally within the 2σ band, the number of loops exhibits strong differences between the data and model in the tail. This difference peaks at more than 5 standard deviations at scales of approximately 5 degrees and more. We note that the distribution of the Betti numbers is manifestly non Gaussian at these scales and thresholds (c.f. (Pranav 2022)).

3.1.3. Significance of combined thresholds and resolutions

Table 1 presents the p -values from the χ^2 statistics for b_0 , b_1 , and EC_{rel} for the PR4 dataset. EC_{rel} is the alternating sum of the Betti numbers, and indicates the Euler characteristic of the excursion set relative to the mask. The p -values for the PR3 dataset based on SMICA maps are presented in the Appendix in Table A.1. The first seven rows in the tables present the p -values combining different thresholds for a given resolution, accounting for multiple testing at different thresholds. For both the datasets, the p -values are consistent with the graphs, broadly indicating similar properties. For experiments where the variance is computed separately for the hemispheres, there are significant deviation between data and model around a degree at $FWHM = 80'$ for all the topological quantities. In addition, b_0 exhibits differences for a range of scales $FWHM = 80', 160', 320'$, with b_1 also exhibiting mild differences. In contrast the experiments with common variance exhibit departure between the data and model

in the southern hemisphere at scales of 5 degrees and larger. The differences are most evident in the number of loops, which also affects the EC_{rel} . However, we also note the deviant behavior of b_0 at $FWHM = 320'$ in the northern hemisphere.

To account for multiple testing at various resolutions, the last entry in the tables present the summary p -values combining all the tested thresholds and resolutions. For the experiments with the variance computed separately for the different hemispheres, the summary p -values present significant evidence for non-random deviation for all the topological descriptors in the northern hemisphere. Similarly for the experiments with a common variance computed from the full sky, the southern hemisphere indicates non-random discrepancy between the data and the model for all the topological descriptors, which is mild for b_0 , but significant for b_1 and EC_{rel} .

3.1.4. The effect of normalization

Normalization is an order preserving transformation topologically. This ensures that there is a bijection between the original and the normalized maps, and specifically a correspondence in the dictionary of critical points as well as the order in which they appear in the filtration to form and destroy the topological cycles. This entails that, at the most, an erroneous estimation of mean and variance would induce an offset between the level-sets of the compared maps, without affecting the deeper topological structure of the field. Combined with the fact that there are stark differences between the data and model irrespective of the recipe for normalization, this points to a difference in the topological structure of the observed field with respect to the

Relative homology $-\chi^2$ (empirical) – Separate Variance							
		North			South		
Res	FWHM	b_0	b_1	EC_{rel}	b_0	b_1	EC_{rel}
threshold = 0.90							
1024	10'	0.4083	0.0733	0.1483	0.9917	0.7617	0.8867
512	20'	0.4633	0.0850	0.1650	0.9933	0.8183	0.9933
256	40'	0.0600	0.3350	0.4767	0.3500	0.8167	0.7283
128	80'	0.0367	0.0367	0.0350	0.6617	0.9017	0.9150
64	160'	0.0433	0.0583	0.0733	0.2833	0.7217	0.8500
32	320'	0.0200	0.2150	0.1017	0.5967	0.1033	0.1717
16	640'	0.5600	0.2900	0.4700	0.4283	0.1783	0.2683
summary	N/A	0.0233	0.0533	0.0167	0.5767	0.8767	0.9250

(a)

Relative homology $-\chi^2$ (empirical) – Global Variance							
		North			South		
Res	FWHM	b_0	b_1	EC_{rel}	b_0	b_1	EC_{rel}
threshold = 0.90							
1024	10'	0.4600	0.1467	0.2750	0.5167	0.2567	0.3150
512	20'	0.1917	0.1450	0.1250	0.3783	0.1117	0.1733
256	40'	0.1817	0.3400	0.5217	0.4533	0.0833	0.3233
128	80'	0.0750	0.2383	0.3567	0.1217	0.0400	0.1367
64	160'	0.3383	0.1250	0.2867	0.5150	0.1583	0.5817
32	320'	0.0383	0.2967	0.2617	0.0650	0.0017	0.0000
16	640'	0.8800	0.9617	0.9000	0.3317	0.0167	0.0150
summary	N/A	0.1667	0.6383	0.5283	0.0783	0.0183	0.0000

(b)

Table 1: Table displaying the two-tailed p -values for relative homology obtained from the empirical Mahalanobis distance or χ^2 test, computed from the sample covariance matrices, for different resolutions and smoothing scales for the NPIPE dataset. Panel (a) presents the p -values for experiments where the variance is computed for each hemisphere separately, and panel (b) presents results for experiments where the hemispheres are assigned the variance of full sky. The last entry is the p -value for the summary statistic computed across all resolutions. Marked in boldface are p -values 0.05 or smaller.

simulations at a level deeper than normalization. Appendix A.1 presents a short account of the properties of the distribution of mean and variance for the full sky and the galactic hemispheres. At the level of mean, both the northern and the southern hemispheres are consistent between the data and model, which is reflected in the behavior of the mean in the full sky as well. In contrast, the variance of the northern hemisphere shows stark deviation between observation and simulations, while the variance in the southern hemisphere is consistent between the data and the model. This engenders a variance in the full sky case, which exhibits a mild deviation between the observation and simulations. Due to the evident discrepancy in variance, it is also prudent to treat both the hemispheres as arising from different models, and consequently treat the results from this experimental procedure as more meaningful.

3.2. Quadrants of the sphere

Following the results of the previous section where we detect an anomalous behavior in the hemispheres, in this section, we compare the behavior of the observations and simulations in the different quadrants of the sphere for the PR4 dataset, illustrated in Figure 2, with a view to determine the zone of discrepancy more accurately. In these experiments, we compute the mean and

Relative homology $-\chi^2$ (empirical) – Separate Variance							
		Quad 1			Quad 2		
Res	FWHM	b_0	b_1	EC_{rel}	b_0	b_1	EC_{rel}
threshold = 0.90							
512	20'	0.1800	0.3433	0.2917	0.5617	0.0283	0.0567
256	40'	0.0250	0.3650	0.2233	0.5483	0.5533	0.7467
128	80'	0.4117	0.3267	0.5183	0.4350	0.4767	0.5667
64	160'	0.0050	0.0150	0.0033	0.2867	0.4700	0.6450
32	320'	0.4283	0.1517	0.4067	0.1817	0.4083	0.6050
summary	N/A	0.0017	0.0383	0.0100	0.2767	0.3200	0.2183

(a)

Relative homology $-\chi^2$ (empirical) – Separate Variance							
		Quad 3			Quad 4		
Res	FWHM	b_0	b_1	EC_{rel}	b_0	b_1	EC_{rel}
threshold = 0.90							
512	20'	0.9767	0.6133	0.8833	0.9283	0.6967	0.9700
256	40'	0.8100	0.5233	0.7183	0.2333	0.7300	0.6200
128	80'	0.7983	0.6400	0.8350	0.7683	0.6383	0.7500
64	160'	0.5533	0.4483	0.7083	0.5933	0.6100	0.6267
32	320'	0.1233	0.5200	0.1433	0.2100	0.3617	0.3517
summary	N/A	0.7433	0.6200	0.4683	0.4717	0.6917	0.5533

(b)

Table 2: Table displaying the two-tailed p -values for relative homology obtained from the empirical Mahalanobis distance or χ^2 test, computed from the sample covariance matrices, for different resolutions and smoothing scales for the maps in different quadrants of the sphere for the NPIPE dataset. Panel (a) presents the p -values for experiments where the variance is computed for each hemisphere separately, and panel (b) presents results for experiments where the hemispheres are assigned the variance of full sky. The last entry is the p -value for the summary statistic computed across all resolutions. Marked in boldface are p -values 0.05 or smaller.

the variance locally from the quadrants for map-normalization. We restrict ourselves to the analysis of scales represented by $FWHM = 20, 40, 80, 160, 320$. Our choice of scales is determined by the fact that, on the larger scales, statistics on smaller sections of the sphere may not be reliable due to the low numbers involved, while the smaller scales have significant computational overhead.

Figure 6 presents the graphs for the Betti numbers while Table 2 presents the p -values computed from the empirical χ^2 test for the different quadrants, based on 600 simulations. Examining the graphs, the first quadrant stands out due to the maximum deviation for b_1 at $FWHM = 160'$, with a significance of more than 3.8σ . The p -values presented in Table 2 corroborate the fact that the northern hemisphere exhibits anomalous behavior with respect to the simulations, where the source of the discrepancy is clearly associated with the first quadrant. The summary p -values combining all thresholds and resolutions indicate a strong non-random deviation between data and model in the first quadrant, which is the strongest for b_0 . Interesting to note is that the deviations between the data and model for the quadrants have shifted to a slightly higher resolution of $FWHM = 160'$, where also b_0 exhibits the strongest deviations. In comparison, the quadrants of the southern hemisphere exhibit no difference with respect to the model, consistent with the observation that the southern Galactic hemisphere is congruent with the standard model, when the maps are normalized by local mean and variance.

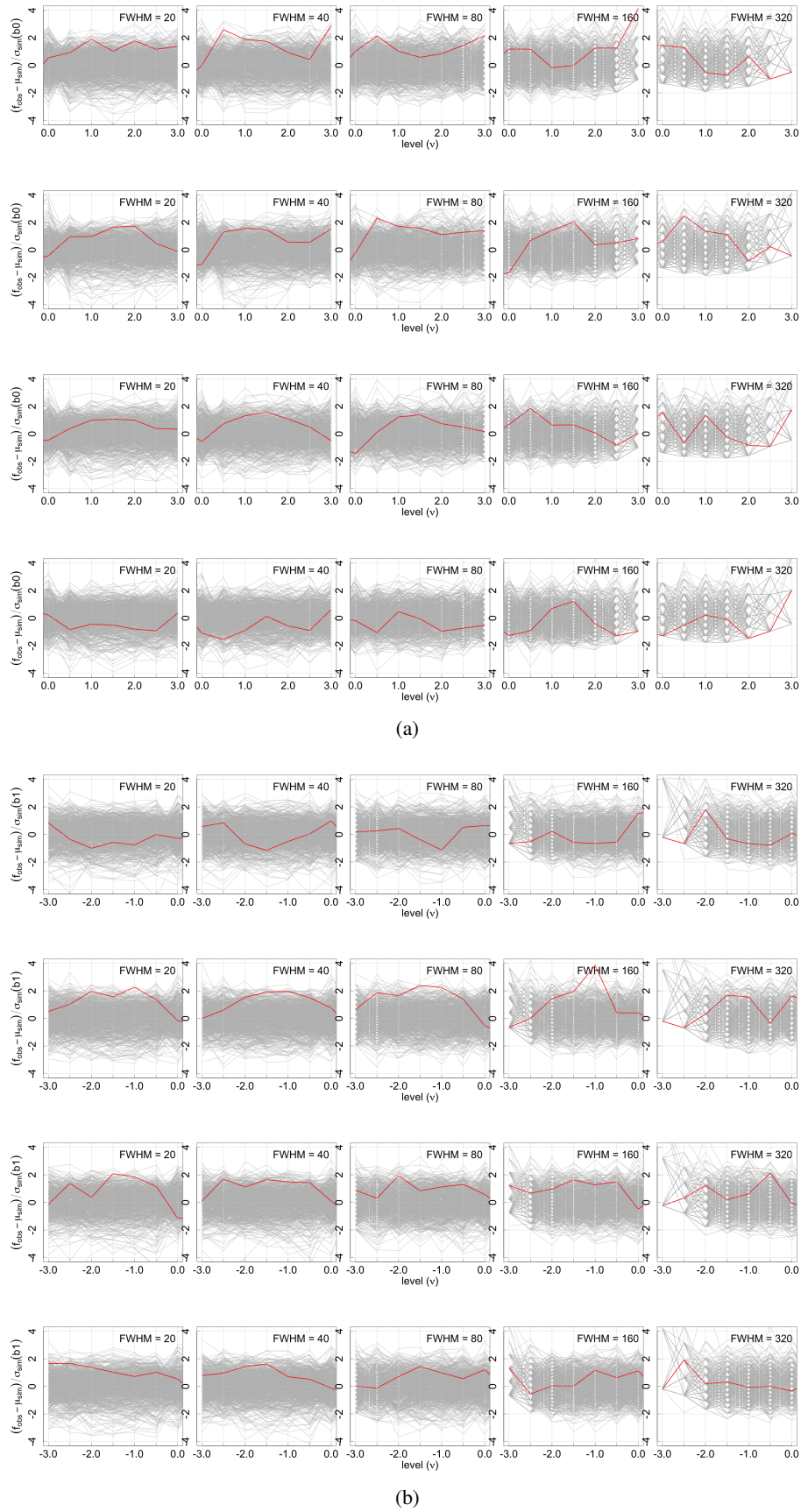


Fig. 6: Graphs of b_0 and b_1 for the different quadrants of the sphere for a range of smoothing scales with Gaussian $FWHM = 20', 40', 80', 160', 320'$. Panel (a) presents the graphs for b_0 while panel (b) presents the graphs for b_1 . The values for the different quadrants are presented from top to bottom, while the scale increases from left to right.

3.3. Comparison with earlier results in literature

Local hemisphere variance: In the experiments with variance computed locally from the hemispheres, the most striking feature is the significant deviation at around a degree in the northern hemisphere. We have noticed hints of this degree-scale deviation in the full sky analysis reported in Pranav (2022), where we report a 2.96σ deviation in the PR3 dataset at $FWHM = 80'$. The PR4 dataset at this scale exhibits a 2.2σ deviation. Due to a weak display of anomaly in the PR4 dataset, we rejected it in view of the larger scales exhibiting stronger anomalies statistically.

We find a similar phenomenon in the reported investigations on the WMAP data in literature. Park (2004) and Eriksen et al. (2004b) pioneered the investigation of genus statistics of WMAP CMB data. While Park (2004) restricted to small sub-degree scales, Eriksen et al. (2004b) performed a multi-scale topogeometrical investigation, spanning a range of sub-degree small scales to super-degree large scales. Due to its multi-scale analysis, as well as the fact that it is performed on WMAP data, and represents independent evidence, we find Eriksen et al. (2004b) an excellent source for comparison with our results. Figure 4 of Eriksen et al. (2004b) presents the Minkowski functional curves for the WMAP data smoothed at $FWHM = 1.28$ deg, where the genus in the positive threshold range is deviant from the simulations at more than 2σ . This is more evident in the Figure 5 of Eriksen et al. (2004b), where the MFs and the skeleton length are presented for a range of smoothing scales. We notice a discrepancy in the genus between observations and simulations at more than 2σ for positive thresholds for a range of scales, most prominently around 1.28 deg and 1.70 deg. The genus for the negative thresholds shows no anomaly at these scales. This also results in the suppression of the signal from the positive threshold anomaly in the χ^2 -statistic for genus. Simultaneously, for the larger scales of approximately 5 degrees, the genus at negative thresholds is deviant by more than 3σ , and therefore, like in our case in Pranav (2022), Eriksen et al. (2004b) also do not deem the degree scale deviation as significant in view of the anomaly at larger scales. In the same paper, Figure 10 shows that the asymmetry parameter between negative and positive thresholds for the genus is weakly correlated. This is experimental evidence in support of the theoretical fact that the different Betti numbers, which dominate the genus at different thresholds, are independent, which further motivates the case of examining the Betti numbers separately, in addition to their linear combination reflected in the genus. Our experiments further support this observation, as the Betti numbers of the hemispheres reveal a difference in their topological properties, which is the source of weak deviation observed in the full sky analysis for the Betti numbers as well as the associated genus statistics in both the Planck and WMAP data, which has been overlooked and not given due attention before.

Global variance: Assigning the global variance to the hemispheres gives rise to discrepant behavior between observations and simulations in the southern hemisphere, specifically for the loops at scales of roughly 5 degrees and larger. The observed discrepancy stands at approximately 5 standard deviations. We have observed the hints of this phenomenon in the full sky analysis as well, where we report a difference of 3.9 standard deviation in the number of loops between the observations and simulations at this scale (Pranav 2022). The source of this deviation is linked to the strongly deviant behavior of loops in the southern hemisphere. Moreover, this phenomenon is observed in the WMAP data also, where the genus at negative thresholds exhibits large

deviations from the simulations at these scales (Eriksen et al. 2004b).

4. Discussions and Conclusion

In this paper, we presented a multi-scale analysis of the topological properties of the CMB temperature maps in small sectors of the sky, including hemispheres and quads, with an aim to investigate the veracity of the postulate of statistical isotropy. This is in continuation of the experiments performed in Pranav et al. (2019a), Pranav (2022), and Pranav (2021a), where we report on the full sky properties of the temperature fluctuation maps. We have employed tools emanating from homology and its hierarchical extension persistent homology, which form the foundations of computational topology (Edelsbrunner et al. 2002; Edelsbrunner & Harer 2010; Pranav et al. 2017).

We have found various anomalous signatures in the topology of the temperature fluctuations in the normalized maps in the different hemispheres defined in the Galactic coordinates. The discovered anomalous signatures in the different hemispheres depend on the section of the sky adopted for computing the mean and variance for normalizing the maps. For experiments where the hemispheres are assigned local mean and variance for normalization, we find that the northern hemisphere exhibits significant deviations between the data and the model, most prominently at scales of roughly a degree, in which case the coincidence between the scale of the anomaly and the horizon at the epoch of CMB is worth noting. The anomalous signatures in this case are more prominent for topological components, however the topological holes also exhibit anomalous behavior. In contrast, the southern hemisphere exhibits remarkable consistency with the standard model simulations. For the experiments where the hemispheres are assigned a global mean and variance computed from the masked full sky, the southern hemisphere exhibits strongly anomalous behavior with respect to the standard model simulations at scales of roughly 5 degrees and more.

Noting that the variance of the northern hemisphere is starkly different from the simulations, while the variance of the southern hemisphere is strongly consistent with the model, it maybe prudent to treat the hemispheres as arising from different models at the level of normalization. Consequently, the results from the experiments where the variance is computed locally from the hemispheres may be a more accurate reflection of reality than the experiments where the hemispheres are assigned a global variance for normalization. In view of this, the degree-scale anomalies in the behavior of the topological components in the northern hemisphere maybe a stronger and fairer indicator of the ground-truth, compared to the larger scale anomalies in the topological loops in the southern hemisphere, which may possibly be an instance of an artifact of data treatment. Taking hints from the experiments on the hemispheres, we further tested the quadrants of the sphere assigning local variance for normalization. In this case, we find that the first quadrant exhibits significantly anomalous behavior with respect to the simulations.

Despite possible offsets due to an erroneous estimation of mean and variance, considering the fact that normalization is an order preserving transformation, and that the anomalies persist irrespective of the recipe adopted for normalization, this points to deeper differences in the stochastic structure of the observed and simulated CMB fields, at a level beyond normalization and offset effects. The fact that the deviations persist in the χ^2 -tests, which takes into consideration all the thresholds and resolutions, is another compelling argument against the deviations being engendered by offset effects. However, to avoid and mitigate any

such effects, in future research we will present a comparison of topology directly in the space of persistence diagrams, which encode consolidated information about all level-sets. Preliminary inroads in this direction have been made in terms of modeling persistence diagrams directly, with an analysis of the Galactic hemispheres in Adler et al. (2017).

An agnostic interpretation of these data characteristics points to a departure from statistical isotropy in the CMB maps, however further work is required to convincingly ascribe the source of the anomalies to a genuinely cosmological effect, unaccounted foreground effect, or merely systematic effects. Regarding noise and systematics, there is an important point to consider from first principles. The PR4 dataset purportedly has lower level of systematics and noise compared to the PR3 dataset. If this is the ground truth, and if the anomalous signals we have discovered are real, their significance should increase from PR3 to PR4 datasets. We notice this trend for the NILC and SEVEM maps, but the opposite trend for C-R and SMICA maps, which makes any assessment about the origin of the signals inconclusive. Also important to note is that the slightly differing results for the different maps in PR3 indicate the sensitivity of our methodology to the details of the component separation pipeline, and maybe considered as a framework for bench-marking. In the context of foregrounds, the recently discovered foreground effect by Hansen et al. (2023) also deserves a specific mention. They find that there is an effect of deepening of CMB temperature profile extending to a few degrees around nearby large spiral galaxies. While they posit that this foreground effect may provide a possible common explanation for a number of anomalies of different kinds in the CMB, restricting to the topological anomalies, such an effect may generate spurious holes in addition to deepening their temperature profiles. However, we find it difficult to conclude that the aforementioned foreground may account for the novel anomalous signatures presented in this paper, for various reasons. First, the evidence presented in this paper points to strongly anomalous signatures in the hot-spot regions as well, which cannot be explained by deepening of temperature profiles, or creation of spurious cold-spots. Second, the fact that the anomalous number of cold-spots appear in the southern hemisphere when assigning a global variance for normalization, and disappear when normalizing the hemispheres by local variance, points to the fact that the anomalous behavior of the cold-spots in the southern hemisphere may in fact be misleading, and engendered as an artifact of data processing. The third compelling reason is that we find the deviations to be the most significant in the first quad in galactic coordinates, and the foreground map presented in Hansen et al. (2023) appears to be lacking significant foreground contamination in this region. Regardless of the finer details, a crucial point to note from the evidence in this paper is that the disagreement between the data and the model may engender spurious results for all subsequent downstream calculations such as cosmological parameter estimation, as pointed out in Fosalba & Gaztañaga (2021); Yeung & Chu (2022), and may have consequences for the Hubble tension through the related mis-estimation of cosmological parameters.

Acknowledgements

We are indebted to Herbert Edelsbrunner, Rien van de Weygaert, and Robert Adler for discussions and comments that have helped shape the draft. We are grateful to Hans Kristian Eriksen and Geraint F. Lewis for important comments on the draft. PP would also like to acknowledge the important interactions with Reijo Keskitalo and Julian Borill, their

consistent help with questions, and incisive comments on the draft. This work is part of a project that has received funding from the European Research Council (ERC) under the European Union's Horizon 2020 research and innovation programme (grant agreement ERC advanced grant 740021 - ARTHUS, PI: TB). P.P. is currently supported by the Physics of Living Matter Group at the University of Luxembourg, and by the Luxembourg National Research Fund's grants awarded to the PI of the Physics of Living Matter Group (ATTRACT Investigator Grant no. A17/MS/11572821/MBRACE, and CORE Grant no. C19/MS/13719464/TOPOFLUME/Sengupta). We gratefully acknowledge the support of PSMN (Pôle Scientifique de Modélisation Numérique) of the ENS de Lyon, and the Department of Energy's National Energy Research Scientific Computing Center (NERSC) at Lawrence Berkeley National Laboratory, operated under Contract No. DE-AC02-05CH11231, for the use of computing resources.

References

- Adler, R. J., Agami, S., & Pranav, P. 2017, *Proceedings of the National Academy of Sciences*, 114, 11878
- Aluri, P. K., Cea, P., Chingangbam, P., et al. 2023, *Classical and Quantum Gravity*
- Appleby, S., Chingangbam, P., Park, C., Yogendran, K. P., & Joby, P. K. 2018, *Astrophysical Journal*, 863, 200
- Appleby, S., Park, C., Pranav, P., et al. 2022, *The Astrophysical Journal*, 928, 108
- Bennett, C. L., Larson, D., Weiland, J. L., et al. 2013, *Astrophys. J. Suppl.*, 208, 20
- Biagetti, M., Cole, A., & Shiu, G. 2021, *Journal of Cosmology and Astroparticle Physics*, 2021, 061
- Bouchet, F. R., Peter, P., Riazuelo, A., & Sakellariadou, M. 2001, *Phys. Rev. D*, 65, 021301
- Buchert, T., France, M. J., & Steiner, F. 2017, *Classical and Quantum Gravity*, 34, 094002
- Carlsson, G. 2009, *Bulletin of the American Mathematical Society*, 46, 255
- Chingangbam, P., Yogendran, K. P., Joby, P. K., et al. 2017, *Jour. Cos. and Part. Phys.*, 12, 023
- Cisewski-Kehe, J., Fasy, B. T., Hellwing, W., et al. 2022, *Physical Review D*, 106
- Cisewski-Kehe, J., Wu, M., Fasy, B., et al. 2018, in *American Astronomical Society Meeting Abstracts*, Vol. 231, American Astronomical Society Meeting Abstracts #231, 213.07
- Colin, J., Mohayaee, R., Rameez, M., & Sarkar, S. 2019, *Astron. & Astrophysics*, 631, L13
- Cruz, M., Martínez-González, E., Vielva, P., & Cayón, L. 2005, *Mon. Not. Royal Astro. Soc.*, 356, 29
- Dam, L., Lewis, G. F., & Brewer, B. J. 2023, *Monthly Notices of the Royal Astronomical Society*, 525, 231
- Di Valentino, E., Mena, O., Pan, S., et al. 2021, *Classical and Quantum Gravity*, 38, 153001
- Ducout, A., Bouchet, F. R., Colombi, S., Pogosyan, D., & Prunet, S. 2013, *MNRAS*, 429, 2104
- Durrer, R. 1999, *New. Astro. Review*, 43, 111
- Durrer, R. 2015, *Classical and Quantum Gravity*, 32, 124007
- Edelsbrunner, H. & Harer, J. 2010, *Computational Topology: An Introduction*, Applied mathematics (American Mathematical Society)
- Edelsbrunner, H., Letscher, J., & Zomorodian, A. 2002, *Discrete & Computational Geometry*, 28, 511
- Eriksen, H. K., Hansen, F. K., Banday, A. J., Górski, K. M., & Lilje, P. B. 2004a, *Astrophysical Journal*, 605, 14
- Eriksen, H. K., Novikov, D. I., Lilje, P. B., Banday, A. J., & Górski, K. M. 2004b, *Astrophysical Journal*, 612, 64
- Feldbrugge, J., van Engelen, M., van de Weygaert, R., Pranav, P., & Vegter, G. 2019, *Journal of Cosmology and Astroparticle Physics*, 2019, 052–052
- Finelli, F., Gruppiso, A., Paci, F., & Starobinsky, A. A. 2012, *Journal of Cosmology and Astroparticle Physics*, 2012, 049
- Fixsen, D. J., Cheng, E. S., Cottingham, D. A., et al. 1994, *Astrophysical Journal*, 420, 445
- Fosalba, P. & Gaztañaga, E. 2021, *Monthly Notices of the Royal Astronomical Society*, 504, 5840
- Górski, K. M., Hivon, E., Banday, A. J., et al. 2005, *Astrophysical Journal*, 622, 759

- Guth, A. H. & Pi, S.-Y. 1982, *Physical Review Letters*, 49, 1110
- Guth, A. H. & Tye, S.-H. H. 1980, *Physical Review Letters*, 44, 631
- Hansen, F. K., Banday, A. J., Górski, K. M., Eriksen, H. K., & Lilje, P. B. 2009, *The Astrophysical Journal*, 704, 1448
- Hansen, F. K., Boero, E. F., Luparello, H. E., & Garcia Lambas, D. 2023, *Astron. & Astrophysics*, 675, L7
- Harrison, E. R. 1970, *Physical Review D*, 1, 2726
- Heydenreich, S., Brück, B., & Harnois-Déraps, J. 2021, *Astronomy & Astrophysics*, 648, A74
- Jones, B. J. T. 2017, *Precision Cosmology: The First Half Million Years* (Cambridge University Press)
- Kerscher, M., Mecke, K., Schmalzing, J., et al. 2001, *Astron. & Astrophysics*, 373, 1
- Kerscher, M., Schmalzing, J., Buchert, T., & Wagner, H. 1997, in *Research in Particle-Astrophysics*, ed. R. Bender, T. Buchert, P. Schneider, & F. von Feilitzsch, 83
- Kerscher, M., Schmalzing, J., Buchert, T., & Wagner, H. 1998, *Astron. & Astrophysics*, 333, 1
- Komatsu, E. 2010, *Classical and Quantum Gravity*, 27, 124010
- Kono, K. T., Takeuchi, T. T., Cooray, S., Nishizawa, A. J., & Murakami, K. 2020, arXiv e-prints, arXiv:2006.02905
- Land, K. & Magueijo, J. 2005, *Physical Review D*, 72
- Makarenko, I., Bushby, P., Fletcher, A., et al. 2018, *J. Plasma Phys.*, 84, 047303
- Matsubara, T. 2010, *Physical Review D*, 81, 083505
- Mukherjee, S. & Souradeep, T. 2016, *Physical Review Letters*, 116
- Munkres, J. 1984, *Elements of Algebraic Topology*, Advanced book classics (Perseus Books)
- Oayda, O. T. & Lewis, G. F. 2023, *Monthly Notices of the Royal Astronomical Society*, 523, 667
- Ouellette, A., Holder, G., & Kerman, E. 2023, *Monthly Notices of the Royal Astronomical Society*, 523, 5738
- Paci, F., Gruppuso, A., Finelli, F., et al. 2010, *Monthly Notices of the Royal Astronomical Society*, 407, 399
- Park, C., Pranav, P., Chingangbam, P., et al. 2013, *Journal of Korean Astronomical Society*, 46, 125
- Park, C.-G. 2004, *Mon. Not. Royal Astro. Soc.*, 349, 313
- Peebles, P. 1980, *The Large-scale Structure of the Universe*, Princeton series in physics (Princeton University Press)
- Peebles, P. J. E. 1993, *Principles of Physical Cosmology*
- Perivolaropoulos, L. & Skara, F. 2022, *New Astronomy Reviews*, 95, 101659
- Planck Collaboration, Ade, P. A. R., Aghanim, N., et al. 2016, *Astron. & Astrophysics*, 594, A16
- Planck Collaboration, Ade, P. A. R., Aghanim, N., et al. 2014a, *Astron. & Astrophysics*, 571, A1
- Planck Collaboration, Ade, P. A. R., Aghanim, N., et al. 2014b, *Astron. & Astrophysics*, 571, A23
- Planck Collaboration, Aghanim, N., Akrami, Y., et al. 2020a, *Astron. & Astrophysics*, 641, A1
- Planck Collaboration, Akrami, Y., Andersen, K. J., et al. 2020b, *Astron. & Astrophysics*, 643, A42
- Planck Collaboration, Akrami, Y., Ashdown, M., et al. 2020c, *Astron. & Astrophysics*, 641, A7
- Porter, M. A., Feng, M., & Katifori, E. 2023, *Physics Today*, 76, 36
- Pranav, P. 2015, PhD thesis, University of Groningen
- Pranav, P. 2021, *IEEE Signal Processing Magazine*, 38, 130
- Pranav, P. 2021a, arXiv e-prints, arXiv:2101.02237
- Pranav, P. 2021b, arXiv e-prints, arXiv:2109.08721
- Pranav, P. 2022, *Astron. & Astrophysics*, 659, A115
- Pranav, P., Adler, R. J., Buchert, T., et al. 2019a, *Astron. & Astrophysics*, 627, A163
- Pranav, P., Edelsbrunner, H., van de Weygaert, R., et al. 2017, *Mon. Not. Royal Astro. Soc.*, 465, 4281
- Pranav, P., van de Weygaert, R., Vegter, G., et al. 2019b, *Mon. Not. Royal Astro. Soc.*, 485, 4167
- Schmalzing, J. & Buchert, T. 1997, *Astrophysical Journal Letters*, 482, L1+
- Schmalzing, J. & Gorski, K. M. 1998, *Mon. Not. Royal Astro. Soc.*, 297, 355
- Schwarz, D. J., Copi, C. J., Huterer, D., & Starkman, G. D. 2016, *Classical and Quantum Gravity*, 33, 184001
- Secrest, N. J., von Hausegger, S., Rameez, M., Mohayaee, R., & Sarkar, S. 2022, *The Astrophysical Journal Letters*, 937, L31
- Secrest, N. J., von Hausegger, S., Rameez, M., et al. 2021, *The Astrophysical Journal Letters*, 908, L51
- Seljak, U. & Zaldarriaga, M. 1997, *Physical Review Letters*, 78, 2054–2057
- Shivshankar, N., Pranav, P., Natarajan, V., et al. 2016, *IEEE Trans. Vis. Comput. Graph.*, 22, 1745
- Sousbie, T. 2011, *MNRAS*, 414, 350
- Starobinsky, A. A. 1982, *Physics Letters B*, 117, 175
- Telschow, F., Schwartzman, A., Cheng, D., & Pranav, P. 2019, arXiv e-prints, arXiv:1908.02493
- van de Weygaert, R., Vegter, G., Edelsbrunner, H., Jones, B., & et al., P. P. 2011, *Transactions on Computational Science*, XIV, 60
- Wilding, G., Nevenzeel, K., van de Weygaert, R., et al. 2021, *Monthly Notices of the Royal Astronomical Society*, 507, 2968–2990
- Xu, X., Cisewski-Kehe, J., Green, S. B., & Nagai, D. 2018, arXiv:1811.08450 [arXiv:1811.08450]
- Yeung, S. & Chu, M.-C. 2022, *Physical Review D*, 105

Appendix A:

A.1. Distribution characteristics of mean, variance and Betti numbers

In the results presented in the previous sections, we have noticed features in the topological characteristics that exhibit weak to strong dependence on the recipe for computing mean and variance for normalizing the maps. Specifically, computing the mean and variance locally from the hemispheres points to a difference between the data and model in the northern hemisphere, as opposed to the southern hemisphere that shows remarkable consistency with the model. In contrast, computing the variance from the full sky results in a deviation between the data and model for both the hemispheres for some scales.

As the anomalies presented in the previous sections exhibit a dependence on the recipe for computing mean and variance, we examine the histograms of mean and variance of the hemispheres and the full sky at $N = 512$ in Figure A.1. From the figure, we notice the variance of the observation in the northern hemisphere to be less than the variance from all the 600 simulated maps, while the southern sky is consistent with the simulations. As a result, the full sky exhibits mildly anomalous characteristics with respect to the simulations. When examining the mean, it is evident that both the northern and the southern skies are consistent with the simulations. It has also been noted in the literature that at all scales the northern hemisphere exhibits anomalous variance with respect to the simulations, in contrast with the southern hemisphere, which exhibits no deviation Planck Collaboration et al. (2014b). It may therefore be prudent to treat the hemispheres as arising from different models, when computing the mean and variance for normalization.

Figure A.2 presents the histogram of b_0 from the simulations for this threshold and resolution, with the observed value indicated by a red vertical line. It is evident from the histogram that the distribution maybe approximated by a Gaussian distribution.

A.2. PR3 dataset

In this section, we present the graphs and table of p -values for the PR3 dataset. Figure A.3 presents the graphs of the Betti numbers for the maps that are normalized with respect to local mean and variance, while Figure A.4 presents the graphs for normalization where the mean and the variance are computed from the masked full sky. The graphs display consistent characteristics with that of the PR4 dataset presented in the main body of the paper, albeit with higher significance of difference between the data and the model. Table A.1 presents the p -values computed from the χ^2 -statistic. The top seven rows present the χ^2 -statistic computed from the combined level sets for a given resolution, while the bottom row presents the same for the combination of all thresholds at all resolutions. Commensurate with the graphs, the p -values for the PR3 dataset presents higher significance of difference between the data and the model.

Relative homology $-\chi^2$ (empirical) – Separate Variance							
Res	FWHM	North			South		
		b_0	b_1	EC _{rel}	b_0	b_1	EC _{rel}
threshold = 0.90							
1024	10'	0.2400	0.1100	0.1333	0.9667	0.4567	0.4667
512	20'	0.4333	0.2367	0.2867	1.0000	0.8567	0.9667
256	40'	0.0367	0.3267	0.2733	0.0900	0.6767	0.2467
128	80'	0.0000	0.0467	0.0133	0.6533	0.6233	0.8467
64	160'	0.0633	0.0700	0.2333	0.2867	0.2600	0.5067
32	320'	0.1567	0.2467	0.3433	0.8533	0.2467	0.4600
16	640'	0.8167	0.5400	0.6933	0.8733	0.0233	0.0367
summary	N/A	0.0100	0.0867	0.0000	0.5433	0.3967	0.0133

(a)

Relative homology $-\chi^2$ (empirical) – Separate Variance							
Res	FWHM	North			South		
		b_0	b_1	EC _{rel}	b_0	b_1	EC _{rel}
threshold = 0.90							
1024	10'	0.3400	0.1400	0.3100	0.3600	0.1767	0.2333
512	20'	0.4433	0.3233	0.5467	0.2033	0.1533	0.1767
256	40'	0.2067	0.2167	0.5433	0.3333	0.0833	0.2567
128	80'	0.0167	0.3033	0.0867	0.2833	0.0733	0.1867
64	160'	0.2500	0.3033	0.3000	0.5733	0.0933	0.5100
32	320'	0.1500	0.5467	0.5633	0.5067	0.0033	0.0033
16	640'	0.6400	0.7167	0.6500	0.3733	0.0000	0.0000
summary	N/A	0.2200	0.4500	0.4133	0.0667	0.0000	0.0000

(b)

Table A.1: Table displaying the two-tailed p -values for relative homology obtained from the empirical Mahalanobis distance or χ^2 test, computed from the sample covariance matrices, for different resolutions and smoothing scales for the FFP10 dataset. Panel (a) presents the p -values for experiments where the variance is computed for each hemisphere separately, and panel (b) presents results for experiments where the hemispheres are assigned the variance of full sky. The last entry is the p -value for the summary statistic computed across all resolutions. Marked in boldface are p -values 0.05 or smaller.

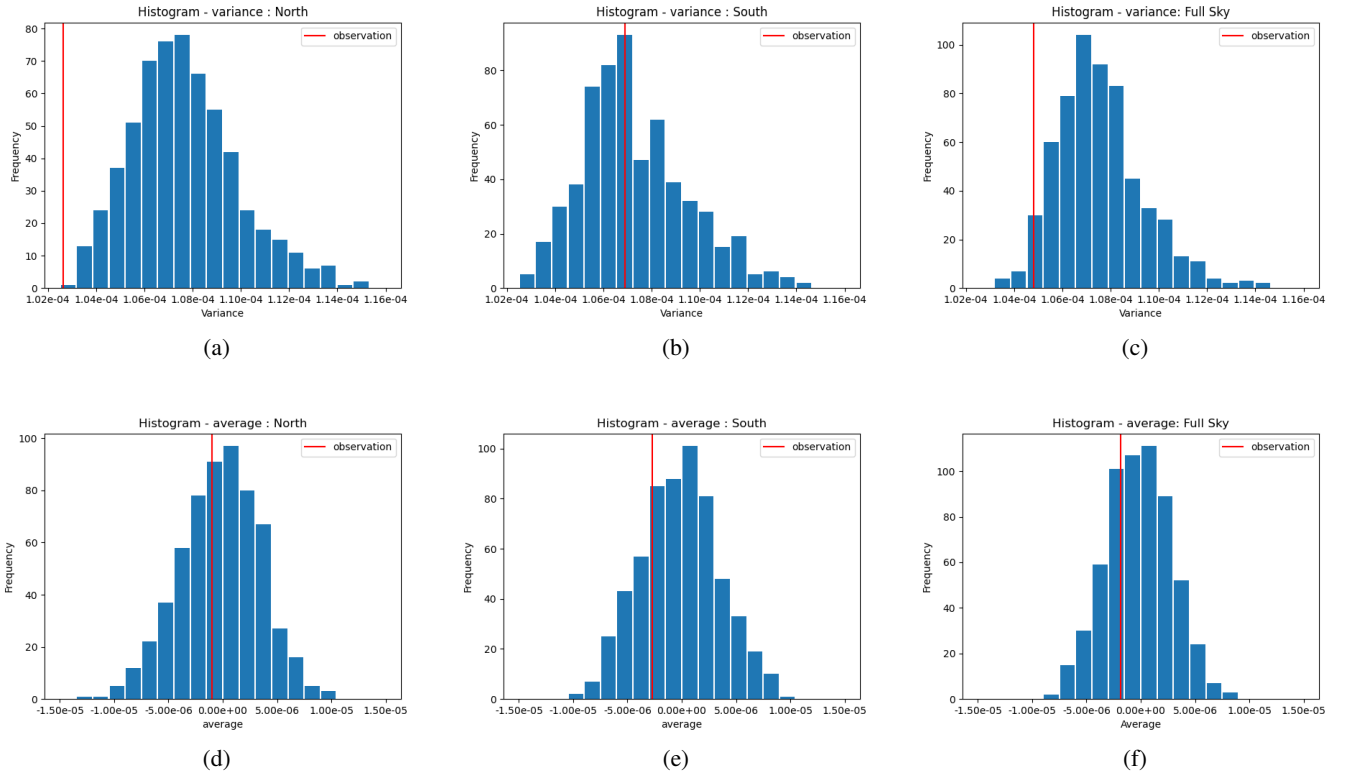


Fig. A.1: Histogram of variance for the north, south and full sky, with the appropriate regions masked. The histograms are computed for the map at $N = 512$.

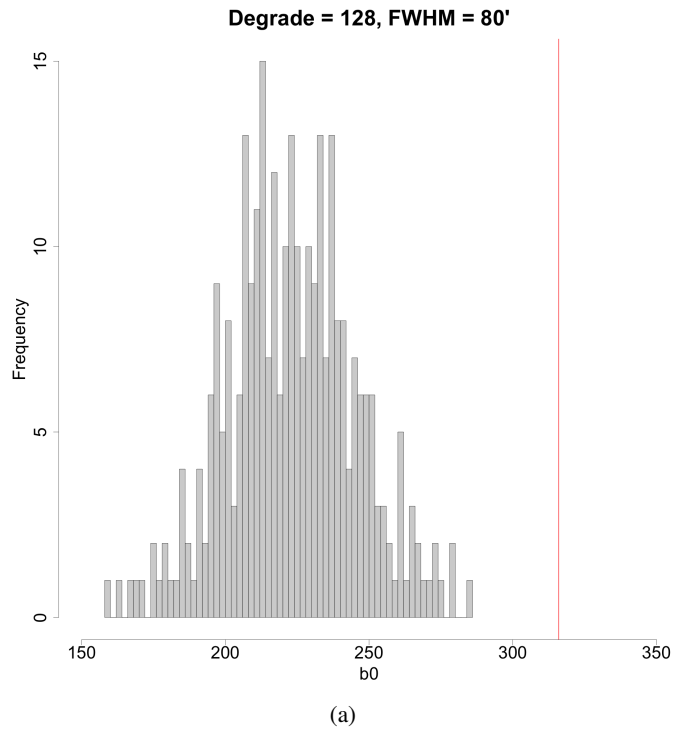


Fig. A.2: Histogram of b_0 values at $\nu = 0.5$ for the PR3 data set at $FWHM = 80'$. The distribution from the simulations indicates a tendency towards a symmetric Gaussian distribution.

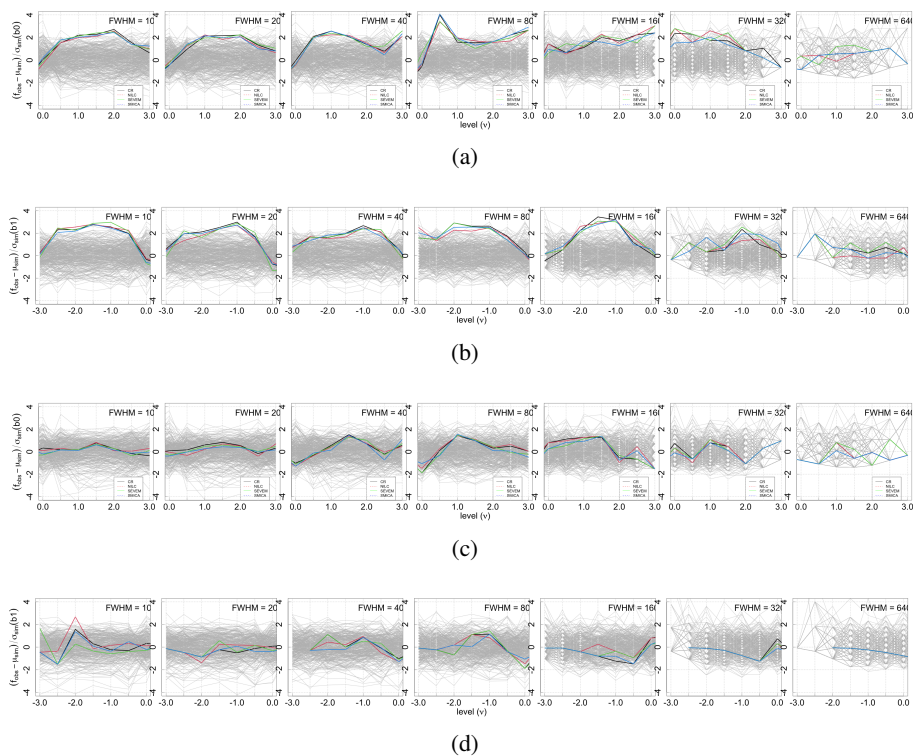


Fig. A.3: Graphs of b_0 and b_1 for the temperature maps for the FFP10 dataset for the northern (top two rows) and the southern hemisphere (bottom two rows). The variance is computed for each hemisphere separately from the unmasked pixels in that hemisphere. The graphs present the normalized differences, and each panel presents the graphs for a range of degradation and smoothing scales. The mask used is the PR3 temperature common mask.

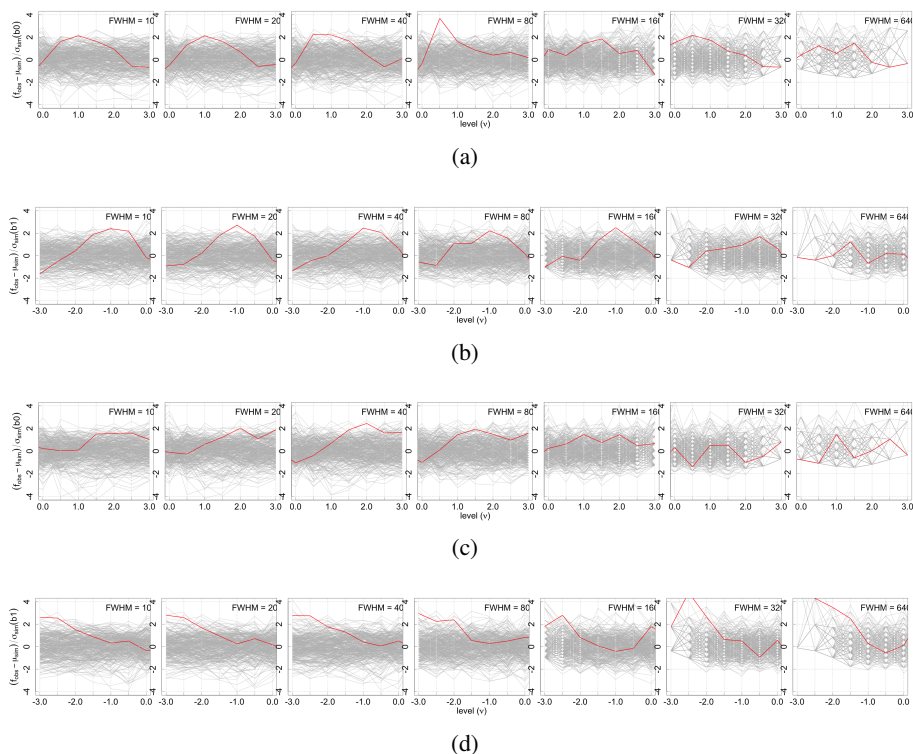


Fig. A.4: Graphs of b_0 and b_1 for the temperature maps for the FFP10 dataset for the northern (top two rows) and the southern hemispheres (bottom two rows). The graphs present the normalized differences, and each panel presents the graphs for a range of degradation and smoothing scales. The variance is computed from the full sky from the unmasked pixels. The mask used is the PR3 temperature common mask.